

Sounding Rocket Observations of Active Region Soft X-Ray Spectra Between 0.5 and 2.5 nm Using a Modified SDO/EVE Instrument

Seth Wieman¹ · Leonid Didkovsky¹ · Thomas Woods² ·
Andrew Jones² · Christopher Moore²

Received: 22 June 2016 / Accepted: 26 September 2016 / Published online: 21 October 2016
© The Author(s) 2016. This article is published with open access at Springerlink.com

Abstract Spectrally resolved measurements of individual solar active regions (ARs) in the soft X-ray (SXR) range are important for studying dynamic processes in the solar corona and their associated effects on the Earth's upper atmosphere. They are also a means of evaluating atomic data and elemental abundances used in physics-based solar spectral models. However, very few such measurements are available. We present spectral measurements of two individual ARs in the 0.5 to 2.5 nm range obtained on the NASA 36.290 sounding rocket flight of 21 October 2013 (at about 18:30 UT) using the *Solar Aspect Monitor* (SAM), a channel of the *Extreme Ultraviolet Variability Experiment* (EVE) payload designed for underflight calibrations of the orbital EVE on the *Solar Dynamics Observatory* (SDO). The EVE rocket instrument is a duplicate of the EVE on SDO, except the SAM channel on the rocket version was modified in 2012 to include a freestanding transmission grating to provide spectrally resolved images of the solar disk with the best signal to noise ratio for the brightest features, such as ARs. Calibrations of the EVE sounding rocket instrument at the *National Institute of Standards and Technology Synchrotron Ultraviolet Radiation Facility* (NIST/SURF) have provided a measurement of the SAM absolute spectral response function and a mapping of wavelength separation in the grating diffraction pattern. We discuss techniques (incorporating the NIST/SURF data) for determining SXR spectra from the

✉ L. Didkovsky
leonid@usc.edu

S. Wieman
wieman@usc.edu

T. Woods
Tom.Woods@lasp.colorado.edu

A. Jones
Andrew.Jones@lasp.colorado.edu

C. Moore
Christopher.Moore-1@colorado.edu

¹ Space Sciences Center, University of Southern California, 835 Bloom Walk, Los Angeles, CA 90089-1341, USA

² Laboratory for Atmospheric and Space Physics, University of Colorado, 1234 Innovation Drive, Boulder, CO 80303-7814, USA

dispersed AR images as well as the resulting spectra for NOAA ARs 11877 and 11875 observed on the 2013 rocket flight. In comparisons with physics-based spectral models using the CHIANTI v8 atomic database we find that both AR spectra are in good agreement with isothermal spectra (4 MK), as well as spectra based on an AR differential emission measure (DEM) included with the CHIANTI distribution, with the exception of the relative intensities of strong Fe xvii lines associated with $2p^6-2p^53s$ and $2p^6-2p^53d$ transitions at about 1.7 nm and 1.5 nm, respectively. The ratio of the Fe xvii lines suggests that the AR 11877 is hotter than the AR 11875. This result is confirmed with analysis of the active regions imaged by *X-ray Telescope* (XRT) onboard *Hinode*.

Keywords Corona, structures · Active regions · Spectrum, X-ray

1. Introduction

Solar soft X-ray (SXR) (0.1 – 10 nm) emissions originate from high-temperature plasma in the solar corona and vary dramatically with solar activity both in terms of band-integrated intensity and spectral distribution (Neupert, 2006). Spectrally resolved measurements in this wavelength range are of significant scientific value and practical utility. They provide valuable diagnostics of the plasma-temperature distribution and elemental abundances in the corona (Del Zanna and Mason, 2014). Such plasma diagnostics are crucial for constraining the various models (Winebarger *et al.*, 2011; Raftery *et al.*, 2013; Asgari-Targhi *et al.*, 2013; Cargill, 2014) describing coronal heating. Understanding these heating mechanisms is currently among the most important problems in solar physics, *e.g.* Klimchuk (2006) and references therein. Also, solar SXR radiation is absorbed in the Earth's mesosphere and lower thermosphere (altitudes between about 80 and 150 km) primarily through photoionization of the major neutral species, O, O₂, and N₂, and as a result, is a primary driver of electron density in the E-region ionosphere. Photoionization cross-sections of these neutral species vary dramatically with wavelength within the SXR band and thus reliable models of E-region peak height, peak density, as well as profile shape require accurate, well-resolved SXR spectra (Sojka *et al.*, 2013). In spite of the importance of solar SXR measurements, relatively few spectrally resolved measurements of quiescent (non-flaring) ARs are available in this wavelength range. Some past measurements include high resolution spectra shortward of 2.5 nm from rocket-borne crystal spectrometers with sufficiently narrow fields of view to isolate individual ARs (Parkinson, 1975; Hutcheon, Pye, and Evans, 1976; Burek *et al.*, 1981). AR SXR spectra from 0.6 to 1.9 nm were also obtained on many occasions throughout the *Solar Maximum Mission* (SMM) from 1980 to 1989 with the onboard *Flat Crystal Spectrometer* (FCS) (Phillips *et al.*, 1982, 1997). Quiescent Sun full-disk irradiance spectra were observed in the 0.25 to 2.5 nm range with a commercial off-the-shelf X-123 avalanche photodiode spectrometer onboard two sounding rocket flights (Caspi, Woods, and Warren, 2015) included on the same flight as the *Solar Aspect Monitor* (SAM) spectra reported in this article. These spectra will soon be available from an identical instrument on the *Miniature X-ray Solar Spectrometer* (MInXSS) cubesat mission (Mason *et al.*, 2016). Additionally, spectrally resolved SXR measurements are available from a number of current or recent missions but only for wavelengths shorter than 0.5 nm, *e.g.* for *Yohkoh* (Kato, Fujiwara, and Hanaoka, 1998), and the *Reuven Ramaty High Energy Solar Spectroscopy Imager* (RHESSI: Smith *et al.*, 2002), or longer than 6 nm on the *Extreme Ultraviolet Variability Experiment* (EVE: Woods *et al.*, 2012).

In the extreme ultraviolet (EUV) spectral range there is a rich history of experiments that have provided spectrally resolved images of the solar corona. Some examples include the *Skylab S082A* slitless spectrograph for 17.1 to 63.0 nm (Tousey *et al.*, 1977), the *Solar EUV Rocket Telescope and Spectrograph* for 23.5 to 45.0 nm (Neupert *et al.*, 1992), and the *Multi-Order Solar EUV Spectrograph* sounding rocket instrument for 30.4 nm (Kankelborg and Thomas, 2001; Fox, Kankelborg, and Thomas, 2010). Related theoretical work includes efforts for optimizing the design and performance of imaging spectrographs (Oktem, Kamalabadi, and Davila, 2013; Davila, 2012). Spectral information has also been extracted from diffraction artifacts (originating from instrument filter support meshes) in images of the solar corona from the *Transition Region and Coronal Explorer* experiment (Lin, Nightingale, and Tarbell, 2001) and the *Atmospheric Imaging Assembly* (Raftery, Krucker, and Lin, 2011).

Broadband measurements in the 0.1–7 nm range from the *XUV Photometer System* (XPS) channels (Woods *et al.*, 2008) on the *Thermosphere, Ionosphere, Mesosphere, Energetics and Dynamics* (TIMED) and the *Solar Radiation and Climate Experiment* (SORCE) and from the *EUV Spectrophotometer* (ESP) channel (Didkovsky *et al.*, 2012) on SDO cover this gap, but determining accurate irradiance values from these measurements requires knowledge of the spectral distribution (solar spectrum) within the band in order to apply the appropriate spectral weighting to the instrument response function – while the XPS and ESP irradiance values are in good agreement under quiet-Sun conditions, they vary by a factor of more than two during active periods, most likely due to the lack of reliable reference spectra for converting raw data to irradiances.

Physics-based theoretical models of solar and stellar plasmas (Del Zanna *et al.*, 2015; Landi *et al.*, 2013; Dere *et al.*, 1997; Warren, Mariska, and Lean, 2001) are widely used for studying solar spectra. These models typically rely on large sets of atomic transition data. In turn, comparisons with solar and stellar observations are used to verify or improve knowledge of such atomic data (Brickhouse, Raymond, and Smith, 1995; Del Zanna, Berrington, and Mason, 2004; Del Zanna, 2006, 2011). The literature concerning ions emitting in the SXR range shows vast disagreement between spectral line intensities from (the limited number of) solar, stellar, and laboratory plasma observations, and those modeled based on available atomic data are often reported (Brown *et al.*, 1998; Laming *et al.*, 2000; Del Zanna, 2011). Such discrepancies are particularly common for the Fe xvii ion with emissions that are dominant in the solar measurements reported in this work.

This article reports solar SXR spectral measurements of two individual active regions (ARs), NOAA numbers 11877 and 11875, observed on a 2013 sounding rocket flight with the EVE/SAM pinhole camera which, for the sounding rocket version of the instrument, includes a freestanding transmission grating that allows spectra to be determined for bright features on the disk with sufficient spatial separation, such as ARs. We describe the analyses required to determine spectra from the wavelength-diffracted images and compare resulting spectra to CHIANTI spectral models and to AR temperature and emission measure maps determined from concurrent *X-ray Telescope* (XRT) measurements. We discuss the potential significance where differences in these comparisons occur.

2. Instrumentation

The SAM channel discussed in detail in Woods *et al.* (2012), Hock *et al.* (2012), and Lin *et al.* (2016) of the EVE on SDO is a pinhole camera with thin-film filters that include Ti, C, and Al layers which limit its sensitivity to wavelengths shorter than about 7.0 nm. The SDO/EVE/SAM instrument provided solar SXR images (Figure 1) from its April 2010

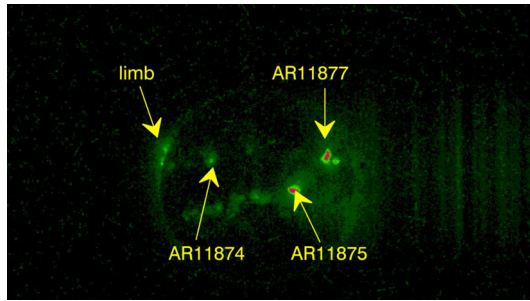


Figure 1 SDO/EVE/SAM image from 21 October 2013 at the time of the reported sounding rocket observations. Several bright ARs are labeled. The image is shown inverted (north is down) as extracted from EVE level 0b data files. This image appears in one corner of the CCD which SAM shares with the EVE *Multiple EUV Grating Spectrometer A* (MEGS-A) channel – some MEGS-A spectral lines (most apparent as bright vertical stripes in the right third of the image) overlap the SAM image.

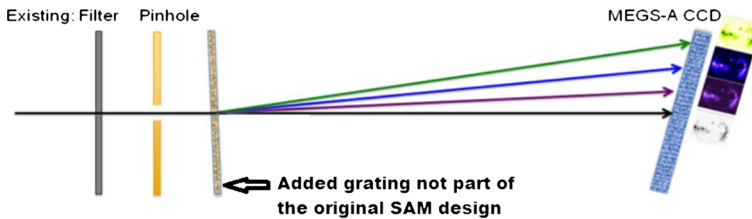


Figure 2 Optical layout of the modified SAM-r instrument. Al and C-Ti-C thin-film filters (in the original design) limit the band pass to wavelengths shorter than about 7 nm. An added freestanding transmission grating allows spectral information to be determined for bright portions (*e.g.* ARs) of the solar image. The SAM-r also has a larger pinhole diameter of 85 μm compared to the SDO/EVE/SAM pinhole of 26 μm . This diagram shows the solar images at each wavelength as being separated for clarity, but these solar images actually overlap with a distinct spectrum for each bright active region.

commissioning until May 2014 when its imaging sensor, an EUV and SXR sensitive CCD shared with the *Multiple EUV Grating Spectrograph* channel A (MEGS-A), suffered a power supply failure.

A sounding rocket version of the SDO EVE instrument is used for periodic underflight calibrations (Chamberlin *et al.*, 2009). This version of the instrument is nominally the same as the one operating onboard SDO, however, in 2012, the rocket instrument SAM channel (hereafter SAM-r, used for the SXR spectral measurements reported in this article) was modified (see Figure 2) to include a freestanding transmission grating to allow spectral information to be determined from sufficiently spaced bright features on the disk image, such as ARs. In contrast to the sensitivity of the method described in Raftery, Krucker, and Lin (2011) to analyze strong solar flares, which produce some CCD saturation, the SAM-r setup allows detection of spectra from individual ARs with about three times larger pinhole diameter of 85 μm compared to the SDO/EVE/SAM pinhole of 26 μm . Between flights of the EVE rocket instrument, an absolute calibration is performed on each of its channels, including SAM-r, at NIST/SURF using Beam Line 2 (BL2). Further information on EVE synchrotron calibrations can be found in Hock *et al.* (2012). EVE calibrations are performed at NIST/SURF using a number of synchrotron electron beam energies ranging from 183 to 408 MeV each providing a different photon flux spectrum. For the purpose of determining an absolute calibration for SAM-r, we use measurements of the 408 MeV beam, which pro-

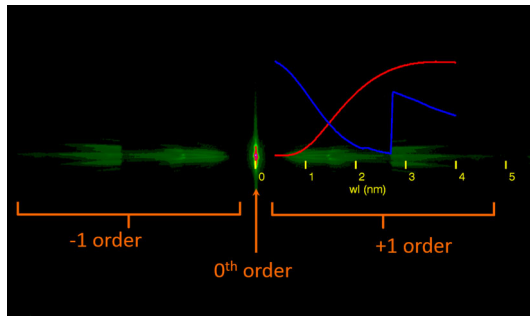


Figure 3 SAM-r image from calibration measurements obtained at the NIST/SURF synchrotron facility using a 408 MeV synchrotron beam. Added annotations include: orange brackets identifying the minus one, zeroth (orange arrow), and plus one grating diffraction orders, a yellow wavelength scale mapping first-order grating wavelength dispersion to position on the CCD image, a red curve showing the relative intensity (energy units) of the 408 MeV synchrotron beam, and a blue curve showing the approximate relative transmission of the combined C-Ti-C and Al thin-film filter layers. The transmission grating supporting mesh also acts as a lower density grating, so there is spectral spreading perpendicular to the primary spectral dispersion in a fan-like shape.

vides the greatest photon fluxes and highest signal-to-noise ratio at the short wavelengths to which SAM-r is sensitive.

A mapping of wavelength dispersion to position on the SAM-r CCD is determined based on NIST/SURF measurements. Figure 3 shows the diffraction pattern observed with SAM-r when illuminated by the highly collimated synchrotron beam with a storage ring electron energy of 408 MeV. The grating dispersion direction is parallel to the horizontal CCD rows to within about 0.25° . In addition to the primary horizontal dispersion from the grating rulings, slight vertical dispersion related to the larger-period grating support mesh is also evident resulting in bands that extend diagonally from the zeroth-order central spot; higher mesh orders correspond to dimmer bands with steeper slopes. Alternating light and dark regions in the plus one- and minus one-order portions of the diffraction pattern are due to the 408 MeV beam spectral shape – shown as a red curve with yellow wavelength scale in Figure 3, with peak photon flux around 3.5 nm – filtered by the SAM C-Ti-C thin-film (an approximate relative filter transmission curve is shown in blue in Figure 3). The yellow wavelength scale is established based on the location of the known Ti filter absorption edge at about 2.75 nm and provides a measure of wavelength dispersion used in the analyses of SAM-r solar images in Section 3.

The synchrotron measurements also provide the SAM-r absolute spectral response function. In the left panel of Figure 4 the SAM-r response in the digital numbers (DN) (DN-dark averaged over multiple rows within the plus first-order portion of the diffraction pattern) is compared to the well-characterized absolute photon flux spectrum of the NIST/SURF 408 MeV beam; uncertainty in the synchrotron beam irradiance is estimated to be about 10 % in the SAM-r wavelength range. The SURF beam flux spectrum (binned to match the wavelength scale of 0.0125 nm/pixel shown in Figure 3) is divided into the measured SAM-r DN profile to provide the spectral response function shown in the right panel of Figure 4, which is used in Section 3 to determine spectral irradiances from the SAM-r solar measurements. The determined response function depends somewhat on the number of rows averaged to form the DN profile (black curve in Figure 4, left panel) as the rows included determine the degree to which the dimmer higher orders related to the grating support mesh (in rows farther from the central peak) affect the average. The response function shown is

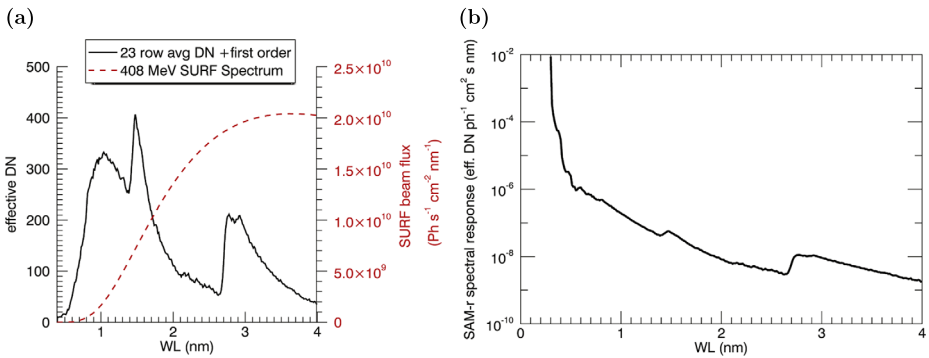


Figure 4 (Left panel) Row-averaged effective response (DN-dark; black curve) of the modified SAM-r instrument to the NIST 408 MeV synchrotron beam with known irradiance spectrum (dashed red curve). The sharp rise in SAM-r response at about 1.43 nm is related to the absorption edge of Ni in the grating and filter support meshes, and the rise at 2.75 nm is related to the Ti thin-film filter (C-Ti-C see Figure 2) edge. (Right panel) SAM-r spectral response function determined by dividing the measured SAM-r DN profile by the SURF beam flux spectrum (binned to match the wavelength scale of 0.0125 nm/pixel shown in Figure 3).

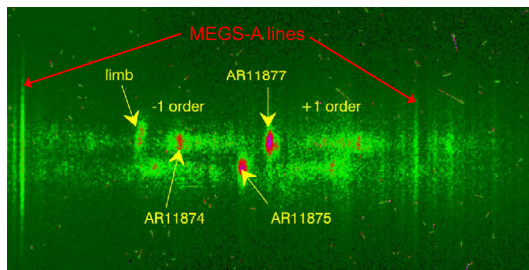


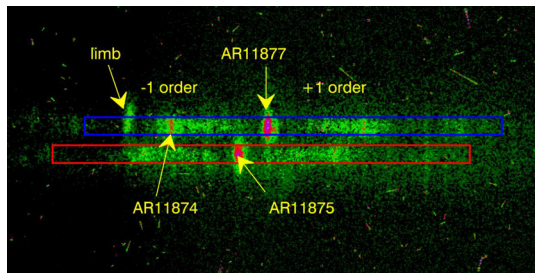
Figure 5 Solar observation made with the SAM-r instrument on flight 36.290 shown inverted (north is down) as extracted from the EVE level 0b data file. First-order diffraction is evident as elongated bright patches on the right and left of the larger ARs (AR 11877 and AR 11875). Residual lines from the MEGS-A channel, which uses the same CCD detector as SAM-r are also visible. Compare this image to the concurrent SDO/EVE/SAM image shown in Figure 1.

based on the averaging of 23 rows. This is the number that we have found most suitable for determining spectra from solar image as will be discussed in the next section.

3. Observations and Analysis

Solar measurements were obtained with the SAM-r channel on two sounding rocket flights, NASA 36.286 on 23 June 2012 at about 19:30 UT, and 36.290 on 21 October 2013 at about 18:00 UT (hereafter 36.286 and 36.290, respectively). The 36.286 flight occurred at the rotation-related minimum of solar irradiance (no visible ARs) with only dim features on the disk that were barely detectable in the zeroth order and did not provide sufficient first-order signal for spectral analysis. Activity levels were higher, however, for the 36.290 flight with several bright ARs including two, NOAA numbers 11877 (S11E61) and 11875 (N07E46), with clearly discernible first-order diffraction patterns. A SAM-r raw image from 36.290 is shown in Figure 5 where the first-order diffraction is evident as elongated bright areas

Figure 6 A clean version of the SAM-r 36.290 image from which MEGS-A lines have been significantly reduced (see discussion in the text). Red and blue rectangles indicate the pixel rows used to analyze the spectra of ARs 11875 and 11877, respectively.



to the left and right of each of these ARs (for contrast, see the concurrent image from the SDO/EVE/SAM in Figure 1 in which these first-order patterns are absent).

Determining spectra from the SAM-r image is complicated by the aforementioned presence of residual vertical lines from the MEGS-A channel, as such lines can potentially introduce false peaks in the first-order diffraction pattern. In an effort to remove these lines, a SAM-r image from the 36.286 flight (with a linear scaling applied to match the background level and the level of the brightest MEGS-A peaks to those of the 36.290 image) is subtracted from the 36.290 raw image. The 36.286 image is suitable for this purpose as it includes the MEGS-A lines while solar features imaged through the SAM pinhole are very dim due to quiet solar conditions during the 2012 flight. MEGS-A lines are far less evident in Figure 6 showing a SAM-r 36.290 image to which this approach has been applied; the image shown is the average of 25 ten-second exposures obtained over the two-minute interval around flight apogee.

Spectral profiles for AR 11877 and 11875 are determined by averaging over the pixel rows highlighted in Figure 6 by the blue and red rectangles, respectively. As alluded to in the discussion as regards the response function in Section 2 and Figure 4, each rectangle consists of 23 rows, a number determined to be optimum in terms of providing the best counting statistics (which improve by including more rows) without expanding the averaging window to include bright features that are unrelated to first-order diffraction of the analyzed AR, and thus distort the extracted spectrum. The objective function for this optimization was a minimization of the asymmetry between plus one and minus one orders based on residual differences in the heights of major plus and minus first-order peaks.

Zeroth-order bright points from other features on the solar disk can effectively contribute an additional non-uniform background to the first-order diffraction pattern for a given AR. For example, it is evident from Figure 6 that AR 11874 falls within the first-order dispersed image of AR 11877. To reduce this background, we subtract from the SAM-r 36.290 image an image obtained at the same time from the SDO/EVE/SAM instrument that has no grating or associated first-order diffraction features. The SDO/EVE/SAM image is scaled to match the intensity of its AR central spot to that of the SAM-r image. Figure 7 illustrates the effect of this subtraction, the gray curve shows the average SAM-r row profile through AR 11877 (*i.e.* the average of the rows within the blue box of Figure 6), the red curve shows the average profile for corresponding pixels of the SDO/EVE/SAM image (Figure 1), and their difference represents the portion of the SAM-r profile related to first-order diffraction.

The first-order spectral profile for AR 11877 (AR 11875), with zeroth-order background subtracted in the above manner, is plotted (black curve) in Figure 8 (Figure 9) using the wavelength scale established from the NIST/SURF calibrations. The zeroth-order central peak of the AR (part of the removed zeroth-order background) has been reinserted as a green curve in the plot. The SAM-r profile does not directly represent a calibrated irradiance spectrum as peak heights are dependent on the SAM-r spectral response. Furthermore,

Figure 7 Subtracting the SDO/EVE/SAM image from the time of the 36.290 rocket flight from the SAM-r image helps to isolate the portion of the SAM-r profile associated with first-order diffraction. Prior to subtraction, the SDO/EVE/SAM image is scaled by a constant to match its central AR peak to that of the SAM-r image (the SAM-r profile is mostly obscured by the SDO/EVE/SAM profile for the central peak and for the limb bright peak centered near pixel -175).

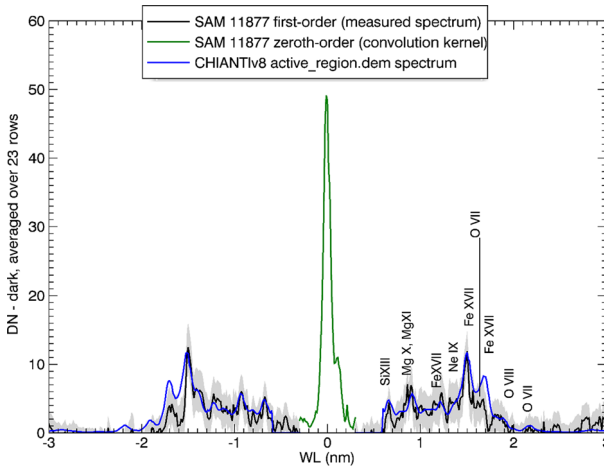
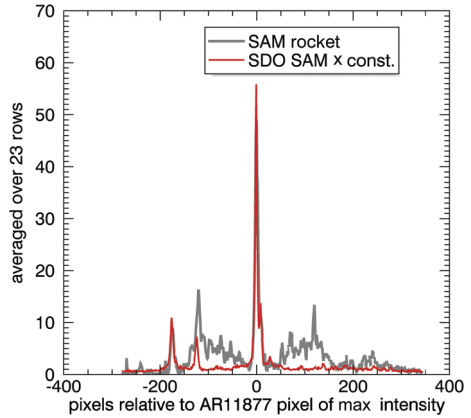


Figure 8 The SAM-r first-order profile (black curve), obtained by averaging rows highlighted in the blue box of Figure 6 and subtracting the background signal related to residual MEGS-A lines and the zeroth-order bright points from other features on the disk, is compared to AR 11877 spectrum modeled with CHIANTI v8 (blue curve) using a file named active_region.dem. The modeled spectrum is fit to the measured profile by folding it with the SAM-r spectral response function and convolving it with the SAM-r zeroth-order AR profile (green curve). Good agreement between the measurement and the model is found for most of the peaks with the exception of the peak near 1.7 nm associated primarily with the $2s^22p^6-2s^22p^53s$ Fe xvii line multiplet. The gray band surrounding the profile represents peak height uncertainty equal to the standard deviation of pixel DN values among the 25 ten-second exposures used to determine the average profile.

the resolution of the profile is limited due to convolution of the spectrum related to the spatial extent of the observed AR (*i.e.*, the dispersed AR images associated with emission lines of similar wavelength tend to overlap) thus most of the profile peaks represent blends of several lines or more. Nonetheless, peaks associated with some known intense spectral lines in this wavelength range (several are listed in Table 1) are discernible and these ions are labeled over the plus first-order portion of the profile on the right side of Figure 8. The gray band surrounding the profile represents peak height uncertainty equal to the standard deviation of pixel DN values among the 25 ten-second exposures used to determine the average profile. To determine the irradiance spectra and estimate the AR temperature distribution we compare the SAM-r spectral profiles with forward-modeled photon spectra using the

Table 1 Wavelengths and transitions of several of the strong lines contributing to spectral peaks observed with SAM-r on 36.290.

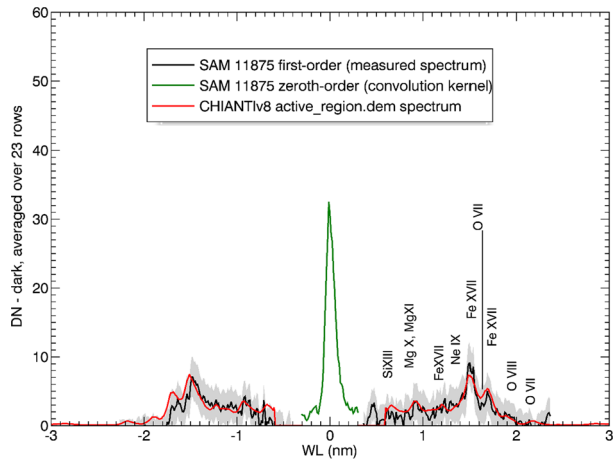
Ion	Transition	WL [\AA]
Si xiii	$1s^2 1s - 1s2p^1 P_1$	6.648
Mg xi	$1s^2 1S_0 - 1s2s^3 S_1$	9.316
Fe xvii	$2s^2 2p^6 1S_0 - 2s^2 2p^5 4d^3 D_1$	12.264
Ne ix	$1s^2 1S_0 - 1s2p^1 P_1$	13.447
Ne ix	$1s^2 1S_0 - 1s2s^3 S_1$	13.699
Fe xvii	$2s^2 2p^6 1S_0 - 2s^2 2p^5 3d^1 P_1$	15.013
Fe xvii	$2s^2 2p^6 1S_0 - 2s^2 2p^5 3d^3 D_1$	15.262
Fe xvii	$2s^2 2p^6 1S_0 - 2s^2 2p^5 3d^3 P_1$	15.453
O viii	$1s^2 S_{1/2} - 3p^2 P_{3/2}$	16.006
Fe xviii	$2s^2 2p^5 2P_{3/2} - 2s^2 2p^4 (^3P) 3s^4 P_{5/2}$	16.072
Fe xvii	$2s^2 2p^6 1S_0 - 2s^2 2p^5 3s^3 P_1$	16.776
Fe xvii	$2s^2 2p^6 1S_0 - 2s^2 2p^5 3s^1 P_1$	17.051
Fe xvii	$2s^2 2p^6 1S_0 - 2s^2 2p^5 3s^3 P_2$	17.096
O viii	$1s^2 S_{1/2} - 2p^2 P_{3/2}$	18.967
O viii	$1s^2 S_{1/2} - 2p^2 P_{1/2}$	18.973
O vii	$1s^2 1S_0 - 1s2s^3 S_1$	22.101

CHIANTI v8 atomic database. For example, in Figure 8, the AR 11877 spectral profile is compared to an AR spectrum as a blue curve (a red curve for AR 11875 in Figure 9) modeled using the “active-region-dem” profile provided with the CHIANTI distribution (scaled by a constant to provide an irradiance spectrum fitting the SAM-r response). For this comparison the CHIANTI spectrum was folded with the SAM response function from NIST/SURF (Figure 4, right), and reduced to the SAM resolution by convolving it with the AR 11877 and AR 11875 zeroth-order profile (green curve in Figures 8 and 9). The observed and modeled spectra agree quite well in general, with most of the model peak heights being within 20 % of the observed peaks, which is well within the error band. One notable exception, however, is the significant difference for the peak around 1.7 nm related primarily to a blend of three Fe xvii lines associated with the $2s^2 2p^6 - 2s^2 2p^5 3s$ transition. Comparing the SAM-r spectral profile for AR 11875 (see Figure 9) to a model spectrum based on the same DEM distribution but with a different constant scaling factor also shows the observed peak heights to be in reasonably good agreement with the model (within the uncertainty band). While the difference in the relative intensity of the Fe xvii peaks at 1.7 nm and 1.5 nm seen in the AR 11877 comparison is also evident for AR 11875, it is not as pronounced.

The Fe xvii peaks at 1.5 nm and 1.7 nm are, even with the degree of convolution of the SAM-r profiles, sufficiently unblended with other elements that their relative heights are not affected by the choice of abundance ratios. Applying different low first ionization potential (FIP) ratios in the CHIANTI model, or even determining the spectrum for the Fe xvii ion only, does not result in a significant difference in the relative heights of the modeled peaks.

It is conceivable, however, that a different representation of the AR temperature structure than the CHIANTI “active-region-dem” distribution might resolve the differences in the modeled relative heights of the Fe xvii peaks compared to the AR 11875 and AR 11877 observations at temperatures of $\log T = 6.4$ and higher. In contrast, temperature maps for the time of the 36.290 flight (see Figure 10) generated based on XRT filter ratio data show

Figure 9 A comparison similar to that in Figure 8, but for AR 11875 with a spectral profile determined from rows within the red box of Figure 6 (the CHIANTI modeled AR spectrum is plotted as a red curve using a file named `active_region.dem`).



little evidence of plasma above about $\log T = 6.35$ for several analyses adopting different abundances and filter combinations.

The XRT Be-thin, Al-mesh, and Al-poly filter images in this analysis were taken near the time of the sounding rocket launch, from 18:03 to 18:04 UT. The analysis was performed on level-1 (using the XRT prep routine) composite images of each filter type with short, medium, and long exposures to increase the dynamic range. Temperature and emission measure maps were created *via* filter ratios of Be-thin/Ti-poly and Be-thin/Al-mesh, using an isothermal approximation in the CHIANTI v8 atomic database and elemental abundances taken from the literature for coronal (Feldman, 1992), hybrid (Schmelz *et al.*, 2012), and photospheric (Caffau *et al.*, 2011) values. The full-Sun synoptic images allow for a direct comparison between ARs 11875 and 11877 inferred physical properties, as any systematic effects in the images will affect both ARs *vs.* narrow field of view XRT images. The XRT results for these two active regions are similar to the peak temperature near $\log T = 6.3$, but AR 11877 is more compact than AR 11875 (see the top panel with the black background in Figure 10), and AR 11877 has more hot pixels than AR 11875 (see bottom panel of Figure 10 with blue curves shifted to the right as compared to the red curves).

Full-disk X-ray spectra reported in Caspi, Woods, and Warren (2015) were obtained using an Amptek X-123 Silicon Drift Diode X-ray spectrometer included with the EVE sounding rocket payload on flights 36.286 and 36.290. However, the spectral resolution of the X-123 is too low in the wavelength range of the 1.5 nm and 1.7 nm Fe xvii lines to give a direct measurement of their relative intensity. Additionally, a two temperature emission measure analysis of the X-ray spectrum from flight 36.290 presented in the Caspi, Woods, and Warren (2015) study suggests a disk-integrated dominant temperature of 2.7 MK ($\log T = 6.43$ at $\log EM = 49.6$, with the EM measured in cm^{-3}) with an additional high-temperature component at 8.7 MK ($\log T = 6.94$ at $\log EM = 47.5$), so the X-123 measurements do not decisively resolve the question of AR temperature either.

On the other hand, the literature concerning Fe xvii X-ray emission lines is extensive and often shows model predictions of the intensity of the $2p^6-3s$ lines, around 1.7 nm, relative to the bright $2p^6-3d$ lines, around 1.5 nm, to be significantly different (by factors of two or more) from what is observed in laboratory or solar plasmas; see *e.g.*, Del Zanna (2011), Laming *et al.* (2000), and Brown *et al.* (1998). The intensity ratio (based on photon units) for the three lines originating from $2p^5-3s$ to those from $2p^5-3d$ is about 1.9 for the CHIANTI v8 AR spectrum, but would need to be about 1.0 to match the AR 11877

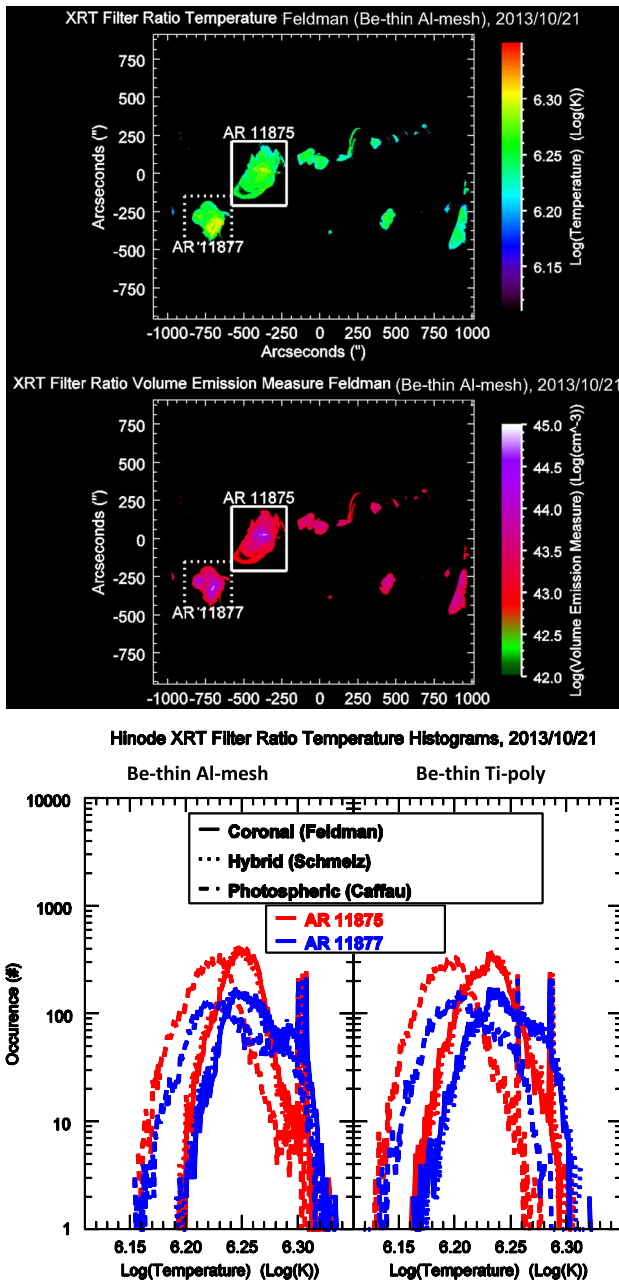


Figure 10 Temperature and emission measure of ARs 11875 and 11877 for the time of the 36.290 flight determined from XRT filter ratio images. Temperature and emission measure maps were created *via* filter ratios of Be-thin/Ti-poly and Be-thin/Al-mesh, using an isothermal approximation in the CHIANTI v8 atomic database and elemental abundances taken from the literature for coronal (Feldman, 1992), hybrid (Schmelz *et al.*, 2012), and photospheric (Caffau *et al.*, 2011) values. In particular, the top panel (on the black background) shows the maps for ARs 11875 and 11877 using the Be-thin/Al-mesh ratio and the coronal elemental abundances from Feldman (1992). The bottom panel presents histograms for the temperature for both ARs (AR 11875 in red color and AR 11877 in blue color) computed from the XRT filter ratios, as shown in the top labels, and the elemental abundances taken from the published values as indicated in the inset at the top.

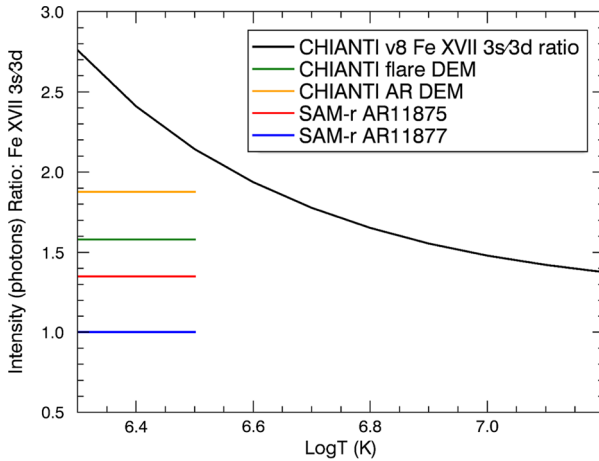


Figure 11 CHIANTI v8 predicted $3s/3d$ intensity ratios (photons) vs. temperature. Horizontal lines compare CHIANTI v8 ratio values based on flare and “active-region-dem” profiles to ratios matching the SAM-r observations for AR 11877 and AR 11875 (these horizontal lines are intended to show discrete ratio values without regard to the abscissa $\text{Log}T$ scale). Because the AR 11877 and AR 11875 ratio values are below those predicted by CHIANTI v8 over the range of temperatures ($\text{Log}T \approx 6.3 - 7.2$) for which Fe xvii ionization fractions are significant, adjusting the modeled temperature structure cannot resolve the aforementioned discrepancies between modeled and observed peak heights near 1.7 nm.

spectral profile, and about 1.40 to match the AR 11875 profile. This $3s/3d$ line intensity ratio is insensitive to electron density, but sensitive to temperature, and based on the CHIANTI v8 “temperature-ratio” diagnostic, over the temperature range $\log T \approx 6.3$ to 7.2 for which the Fe xvii ion fraction is significant, this ratio only varies from about 2.7 to about 1.4 (Figure 11), so in this regard a CHIANTI model spectrum based on a different temperature structure cannot fully resolve these differences (*e.g.* for a spectrum modeled in CHIANTI with the “flare.dem” profile, the $3s/3d$ ratio is only as low as 1.58). However, in the earlier studies (*e.g.* Laming *et al.*, 2000; Raymond and Smith, 1986; Parkinson, 1973) that have included comparisons between model predictions and observations of the Fe xvii $3s/3d$ intensity ratio, a broader range of observed values has been reported. For example, in Laming *et al.* (2000), a compilation of $3s/3d$ intensity ratios observed in solar and stellar plasmas (as well as a laboratory Electron Beam Ion Trap source) spans the range from about 0.8 to about 2.1. While the values for this intensity ratio obtained in our analysis of the SAM rocket data differ from what is predicted by CHIANTI, they are not outside this range of values observed in the past.

Del Zanna (2011) demonstrated that atomic data for the Fe xvii ion presented in Liang and Badnell (2010) (and currently used in CHIANTI v8) reliably predict Fe xvii line intensities for a set of carefully selected solar observations, an important development beyond previous studies, which commonly found predictions based on earlier available atomic data to disagree with solar and stellar observations and explained the differences based on other factors affecting the observed intensities, such as opacity (Saba *et al.*, 1999). Interestingly, some of the earlier atomic data benchmarked in the Del Zanna (2011) study predict $3s/3d$ intensity ratios that closely match our SAM-r observations. For example, Figures 12 and 13 show comparisons of SAM-r spectral profiles (for ARs 11877 and 11875, respectively, as in Figures 8 and 9) with a CHIANTI modeled 4 MK ($\log T = 6.6$) isothermal plasma for which the $3s/3d$ ratios are adjusted to match those predicted (for a 4 MK plasma) based on

ratios from the atomic data of Liang and Badnell (2010) were in good agreement with ratios observed in a carefully selected set of solar measurements using crystal spectrometers. Del Zanna's study indicated that past differences between predicted Fe xvii line ratios and those observed on the Sun could be resolved based on the use of the updated atomic data and that (except for during the peak of large solar flares) other effects, such as opacity, were not needed to explain such reported discrepancies. Our differing results suggest that other processes affecting observed intensities may yet need to be considered, and highlight the need for further spectrally resolved solar measurements in this wavelength range.

Reflights of the EVE sounding rocket could provide further measurements of the type presented here. The *Marshall Grazing Incidence X-ray Spectrograph* (MaGIXS), as reported by Kobayashi *et al.* (2011), sounding rocket will provide complementary narrow field of view (8 arcminute-long slit) spectrally resolved measurements from 0.6 to 2.3 nm, a continuous dataset from a space based observatory over an extended mission including SXR spectra, for which these Fe lines resolved including a range of activity levels could answer this question more conclusively. The adaptability of the SAM-r grating and pinhole camera instrument design to a variety of spacecraft, including small platforms such as CubeSats, and the demonstrated effectiveness of this approach make it a promising candidate for such a mission.

Acknowledgements This work was supported in part by NASA/University of Colorado subcontract 153-5979.

Disclosure of Potential Conflicts of Interest The authors declare that they have no conflicts of interest.

Open Access This article is distributed under the terms of the Creative Commons Attribution 4.0 International License (<http://creativecommons.org/licenses/by/4.0/>), which permits unrestricted use, distribution, and reproduction in any medium, provided you give appropriate credit to the original author(s) and the source, provide a link to the Creative Commons license, and indicate if changes were made.

References

- Asgari-Targhi, M., Van Ballegooijen, A.A., Cranmer, S.R., DeLuca, E.E.: 2013, *Astrophys. J.* **773**(2), 111. [DOI](#).
- Bhatia, A.K., Doschek, G.A.: 1992, *At. Data Nucl. Data Tables* **52**(1), 1. [DOI](#).
- Brickhouse, N.S., Raymond, J.C., Smith, B.W.: 1995, *Astrophys. J.* **97**, 551. [DOI](#).
- Brown, G.V., Beiersdorfer, P., Liedahl, D.A., Widmann, K., Kahn, S.M.: 1998, *Astrophys. J.* **502**(2), 1015. [DOI](#).
- Burek, A.J., Barrus, D.M., Blake, R.L., Fenimore, E.E.: 1981, *Astrophys. J.* **243**, 660.
- Caffau, E., Ludwig, H.G., Steffen, M., Freytag, B., Bonifacio, P.: 2011, *Solar Phys.* **268**(2), 255. [DOI](#).
- Cargill, P.J.: 2014, *Astrophys. J.* **784**(1), 49. [DOI](#).
- Caspi, A., Woods, T.N., Warren, H.: 2015, *Astrophys. J. Lett.* **802**, L2. [DOI](#).
- Chamberlin, P.C., Woods, T.N., Crotser, D.A., Eparvier, F.G., Hock, R.A., Woodraska, D.L.: 2009, *Geophys. Res. Lett.* **36**(5), L05102. [DOI](#).
- Davila, J.M.: 2012, In: *AAS Slitless Spectroscopy Meeting Abstracts*, 220.
- Del Zanna, G.: 2006, *Astron. Astrophys.* **459**(1), 307. [DOI](#).
- Del Zanna, G.: 2011, *Astron. Astrophys.* **536**, A59. [DOI](#).
- Del Zanna, G., Mason, H.E.: 2014, *Astron. Astrophys.* **565**, A14. [DOI](#).
- Del Zanna, G., Berrington, K.A., Mason, H.E.: 2004, *Astron. Astrophys.* **422**(2), 731. [DOI](#).
- Del Zanna, G., Dere, K.P., Young, P.R., Landi, E., Mason, H.E.: 2015, *Astron. Astrophys.* **582**, A56. [DOI](#).
- Dere, K.P., Landi, E., Mason, H.E., Monsignor Fossi, B.C., Young, P.R.: 1997, *Astron. Astrophys. Suppl.* **125**(1), 149. [DOI](#).
- Didkovsky, L., Judge, D., Wieman, S., Woods, T.N., Jones, A.: 2012, *Solar Phys.* **275**, 179. [DOI](#).
- Feldman, U.: 1992, *Phys. Scr.* **46**(3), 202. [DOI](#).
- Fox, J.L., Kankelborg, C.C., Thomas, R.J.: 2010, *Astrophys. J.* **719**(2), 1132. [DOI](#).

- Hock, R.A., Chamberlin, P.C., Woods, T.N., Crotser, D., Eparvier, F.G., Woodraska, D.L., Woods, E.C.: 2012, *Solar Phys.* **275**, 145. DOI.
- Hutcheon, R.J., Pye, J.P., Evans, K.D.: 1976, *Mon. Not. Roy. Astron. Soc.* **175**(3), 489.
- Kankelborg, C.C., Thomas, R.J.: 2001, In: *SPIE* **4498**, 16.
- Kato, T., Fujiwara, T., Hanaoka, Y.: 1998, *Astrophys. J.* **492**(2), 822. DOI.
- Klimchuk, J.A.: 2006, *Solar Phys.* **234**(1), 41. DOI.
- Kobayashi, K., Cirtain, J., Golub, L., Winebarger, A., Hertz, E., Cheimets, P., Caldwell, D., Korreck, K., Robinson, B., Reardon, P., Kester, T.: 2011, In: *SPIE Optical Engineering and Applications Conf. Ser.* **81471M**.
- Laming, J.M., Kink, I., Takacs, E., Porto, J.V., Gillaspay, J.D., Silver, E.H., Schnopper, H.W., Bandler, S.R., Brickhouse, N.S., Murray, S.S., Barbera, M.: 2000, *Astrophys. J. Lett.* **545**(2), L161. DOI.
- Landi, E., Young, P.R., Dere, K.P., Del Zanna, G., Mason, H.E.: 2013, *Astrophys. J.* **763**, 86. DOI.
- Liang, G.Y., Badnell, N.R.: 2010, *Astron. Astrophys.* **518**, A64. DOI.
- Lin, A.C., Nightingale, R.W., Tarbell, T.D.: 2001, *Solar Phys.* **198**(2), 385. DOI.
- Lin, C.Y., Bailey, S.M., Jones, A., Woodraska, D., Caspi, A., Woods, T.N., Eparvier, F.G., Wieman, S.R., Didkovsky, L.V.: 2016, *J. Geophys. Res.* **121**, 1. DOI.
- Mason, J.P., Woods, T.N., Caspi, A., Chamberlin, P.C., Moore, C., Jones, A., Kohnert, R., Li, X., Palo, S., Solomon, S.: 2016, *J. Spacecr. Rockets* **53**(2), 328. DOI.
- Neupert, W.M., Epstein, G.L., Thomas, R.J., Thompson, W.T.: 1992, *Solar Phys.* **137**(1), 87. DOI.
- Neupert, W.M.: 2006, *Adv. Space Res.* **37**(2), 238. DOI.
- Oktem, F.S., Kamalabadi, F., Davila, J.M.: 2013, In: *IEEE International Conference on Acoustics, Speech and Signal Processing* **2169**.
- Parkinson, J.H.: 1973, *Astron. Astrophys.* **24**, 215. <http://adsabs.harvard.edu/abs/1973A...24...215P>.
- Parkinson, J.H.: 1975, *Solar Phys.* **42**(1), 183. DOI.
- Phillips, K.J.H., Fawcett, B.C., Kent, B.J., Gabriel, A.H., Leibacher, J.W., Wolfson, C.J., Acton, L.W., Parkinson, J.H., Culhane, J.L., Mason, H.E.: 1982, *Astrophys. J.* **256**, 774.
- Phillips, K.J.H., Greer, C.J., Bhatia, A.K., Coffey, I.H., Barnsley, R., Keenan, F.P.: 1997, *Astron. Astrophys.* **324**, 381.
- Raftery, C.L., Krucker, S., Lin, R.P.: 2011, *Astrophys. J. Lett.* **743**, L27. DOI.
- Raftery, C.L., Bloomfield, D.S., Gallagher, P.T., Seaton, D.B., Berghmans, D., De Groof, A.: 2013, *Solar Phys.* **286**(1), 111. DOI.
- Raymond, J.C., Smith, B.W.: 1986, *Astrophys. J.* **306**, 762.
- Saba, J.L.R., Schmelz, J.T., Bhatia, A.K., Strong, K.T.: 1999, *Astrophys. J.* **510**(2), 1064. DOI.
- Schmelz, J.T., Reames, D.V., von Steiger, R., Basu, S.: 2012, *Astrophys. J.* **755**(1), 7. DOI.
- Smith, D.M., Lin, R.P., Turin, P., Curtis, D.W., Primbsch, J.H., Campbell, R.D., Abiad, R., Schroeder, P., Cork, C.P., Hull, E.L., Landis, D.A., Madden, N.W., Malone, D., Pehl, R.H., Raudorf, T., Sangsingkeow, P., Boyle, R., Banks, I.S., Shirey, K., Schwartz, R.: 2002, *Solar Phys.* **210**(1), 33. DOI.
- Sojka, J.J., Jensen, J., David, M., Schunk, R.W., Woods, T., Eparvier, F.: 2013, *J. Geophys. Res.* **118**(8), 5379. DOI.
- Tousey, R., Bartoe, J.D., Brueckner, G.E., Purcell, J.D.: 1977, *Appl. Opt.* **16**(4), 870.
- Warren, H.P., Mariska, J.T., Lean, J.: 2001, *J. Geophys. Res.* **106**(A8), 15745. DOI.
- Winebarger, A.R., Schmelz, J.T., Warren, H.P., Saar, S.H., Kashyap, V.L.: 2011, *Astrophys. J.* **740**(1), 2. DOI.
- Woods, T.N., Chamberlin, P.C., Peterson, W.K., Meier, R.R., Richards, P.G., *et al.*: 2008, *Solar Phys.* **250**(2), 235. DOI.
- Woods, T.N., Eparvier, F.G., Hock, R., Jones, A.R., Woodraska, D., Judge, D., Didkovsky, L., Lean, J., Mariska, J., Warren, H., *et al.*: 2012, *Solar Phys.* **275**, 115. DOI.
- Young, P.R., Del Zanna, G., Landi, E., Dere, K.P., Mason, H.E., Landini, M.: 2003, *Astrophys. J.* **144**(1), 135. DOI.